



Quantifying suspended solids in small rivers using satellite data

Celso M. Isidro^{a,*}, Neil McIntyre^a, Alex M. Lechner^{a,b}, Ian Callow^{a,c}

^a Centre for Water in the Minerals Industry, Sustainable Minerals Institute, The University of Queensland, St. Lucia Campus, QLD 4072, Australia

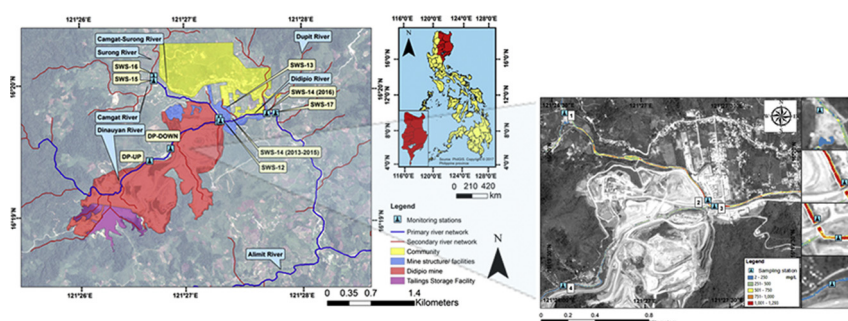
^b School of Environmental and Geographical Sciences, Faculty of Science, University of Nottingham Malaysia Campus, Jalan Broga, Semenyih 43500, Malaysia

^c Rio Tinto Limited, 123 Albert St., Brisbane City, QLD 4000, Australia

HIGHLIGHTS

- Applicability of VHR satellite images in suspended solids monitoring in 4–10 m wide rivers
- Empirical modelling between surface reflectance and total suspended solids (TSS)
- Investigation of inter-station and inter-year variations of pixel reflectance values
- Investigation of spectral bands that accurately represent TSS in shallow mountain rivers
- Calibration of a satellite image into a thematic map of TSS

GRAPHICAL ABSTRACT



ARTICLE INFO

Article history:

Received 17 November 2017

Received in revised form 27 February 2018

Accepted 2 April 2018

Available online xxxx

Editor: D. Barcelo

Keywords:

Total suspended solids

Turbidity

Empirical modelling

Surface reflectance

Small-scale mining

Philippines

ABSTRACT

The management of suspended solids and associated contaminants in rivers requires knowledge of sediment sources. In-situ sampling can only describe the integrated impact of the upstream sources. Empirical models that use surface reflectance from satellite images to estimate total suspended solid (TSS) concentrations can be used to supplement measurements and provide spatially continuous maps. However, there are few examples, especially in narrow, shallow and hydrologically dynamic rivers found in mountainous areas. A case study of the Didipio catchment in Philippines was used to address these issues. Four 5-m resolution RapidEye images, from between the years 2014 and 2016, and near-simultaneous ground measurements of TSS concentrations were used to develop a power law model that approximates the relationship between TSS and reflectance for each of four spectral bands. A second dataset using two 2-m resolution Pleiades-1A and a third using a 6-m resolution SPOT-6 image along with ground-based measurements, were consistent with the model when using the red band data. Using that model, encompassing data from all three datasets, gave an R^2 value of 65% and a root mean square error of 519 mg L^{-1} . A linear relationship between reflectance and TSS exists from 1 mg L^{-1} to approximately 500 mg L^{-1} . In contrast, for TSS measurements between 500 mg L^{-1} and 3580 mg L^{-1} reflectance increases at a generally lower and more variable rate. The results were not sensitive to changing the pixel location within the vicinity of the ground sampling location. The model was used to generate a continuous map of TSS concentration within the catchment. Further ground-based measurements including TSS concentrations that are higher than 3580 mg L^{-1} would allow the model to be developed and applied more confidently over the full relevant range of TSS.

© 2018 Elsevier B.V. All rights reserved.

* Corresponding author.

E-mail address: celso.isidro@uq.net.au. (C.M. Isidro).

1. Introduction

Remote sensing has often been employed to assess water quality in marine and coastal contexts (Wu et al., 2014); however, its application to inland surface water is generally more difficult. Firstly, the concentrations of suspended and organic materials can vary over short distances and time periods (Gitelson et al., 1993). Secondly, high spatial resolution images are required for extraction of spectral information from small to medium-scale rivers (Wu et al., 2014). Lastly, shallow waters expose the river bottom, which may interfere with readings of surface reflectance. These challenges are addressed in this paper.

TSS measurement levels primarily depend on the texture of the source soil. Soil texture defines the particle size distribution of a soil, which is primarily composed of sand (0.06–2 mm), silt (0.02–0.002 mm) and clay (<0.0002 mm) (Pusch et al., 2012). Topsoil comprises sand-size soil particles (0.05–2 mm) whereas clay (<0.0002 mm) and silts (0.05–0.002 mm) tend to be more abundant in subsoil layers (Tindall and Kunkel, 2009). Sand-size soil particles, when eroded, settle in rivers relatively easily whereas clay and silts, due to their smaller particles, are held in suspension for longer.

The application of satellites to water quality assessment relies on relating solar radiation reflected from the water body, as measured by a sensor on the satellite, to a water quality parameter. While other indices of radiation may be used, surface reflectance is usually applied as it already incorporates corrections for the specific magnitude of solar exatmospheric irradiance in each band and each sensor as well as the sun zenith angle. Surface reflectance can be observed at the visible (blue ~490 nm, green ~520 nm, red ~652 nm) and near-infrared (~840 nm) wavelengths.

Several researchers have demonstrated the strong correlation between surface reflectance and TSS or water turbidity as a generally reliable surrogate of TSS (Han and Rundquist, 2007; Rugner et al., 2013; Wu et al., 2014). For measurements ranging from 4 to 40 NTU, turbidity has been found to be significantly correlated with the green and red bands of surface reflectance measured by ALOS AVNIR-2 (Syahreza et al., 2012) while TSS concentrations between 74 and 600 mg L⁻¹ were observed to have a positive relationship with the Band 2 (near-infrared) surface reflectance measured by MODIS (Wang and Lu, 2010). TSS concentrations between 0 and 500 mg L⁻¹ were found to be well correlated with surface reflectance measured by Landsat in the near-infrared band (Harrington Jr et al., 1992); while a study of the Tapajos River Basin in

the Brazilian Amazon using Landsat found a high correlation between TSS and surface reflectance in the red band (Lobo et al., 2016). Landsat TM red band reflectance was also found to have good correlations with turbidity coming from the Hudson River in New York Harbor (Hellweger et al., 2004). In contrast, a nonlinear relationship between surface reflectance and turbidity or TSS values are found at higher ranges, with the nature of the nonlinearity influenced by the sediments particle size, shape and colour (Baker and Lavelle, 1984). The nonlinear relationship between TSS and surface reflectance is often expressed as exponential model (Harrington Jr et al., 1992), power model (Wang et al., 2012) or a second-order polynomial model (Lodhi et al., 1997).

In general, the spectral signature of water includes a peak surface reflectance between the green and red bands at lower TSS concentrations while the peak shifts towards the near-infrared band or longer wavelengths at higher TSS concentrations (Syahreza et al., 2012). Liew et al. (2003) observed that the surface reflectance of water with TSS concentrations 16 mg L⁻¹ and 1338 mg L⁻¹ peaked at 700 nm and 800 nm respectively. At higher TSS concentrations, these peaks merge and move towards the near-infrared channel. Saturation of surface reflectance can be detected at extreme TSS values typically higher than 7450 mg L⁻¹ (Lodhi et al., 1997; Liew et al., 2003).

The strength of correlation between reflectance and TSS or turbidity may be affected by the reflectance of the river bottom in shallow waters. Han and Rundquist (2007) discuss the separate impacts of bright and dark river bottoms on surface reflectance readings. Their experiment was performed in a tank with 80 cm depth of water. The brightness of the bottom had minimal effect on the surface reflectance in the visible spectrum when the TSS concentration was >100 mg L⁻¹, while at lower TSS concentrations a dark bottom can increase surface reflectance in the blue and green bands. In contrast, surface reflectance readings are attributable purely to TSS in the near-infrared region irrespective of the water depth or TSS concentration. In conclusion, it was suggested that for shallow rivers, the near-infrared band should be used to measure surface reflectance. This is supported by other studies (Wu et al., 2014; Han and Rundquist, 2007) that found that surface reflectance is optimally related to TSS between 700 and 900 nm. However, interferences from protruding rocks and river plants, which are likely in shallow rivers, may be expected even in the near-infrared band.

The application of satellite images to estimating TSS and turbidity values has focused on rivers with widths from 1 to 15 km. For instance, the Tapajos River in Brazil has a downstream width between 10 and

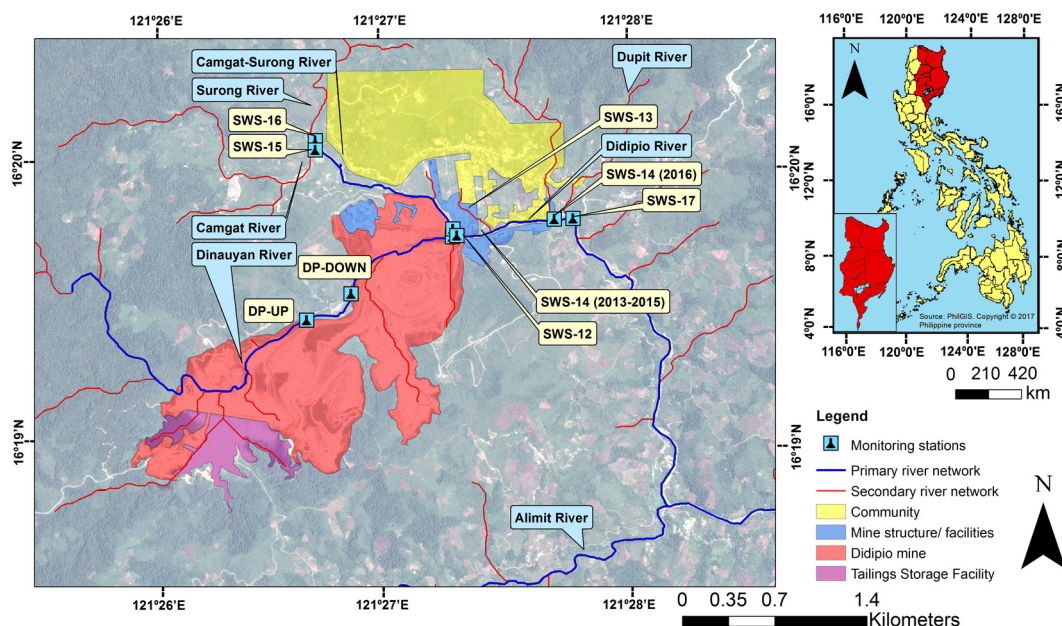


Fig. 1. Locations of selected monitoring stations. Pleiades: © CNES (2013), Distribution Airbus DS/Spot Image.

Table 1
Physical attributes of the monitoring stations based on the 2013–2016 database.

River section	Station	Sampling frequency (days/week)	Width (m)	Average depth (mm)	Mean TSS (mg L ⁻¹)	Std. dev. TSS (mg L ⁻¹)
Dumulag upstream	DP-UP	7	4	250	135	747
Dumulag downstream	DP-DOWN	7	4	250	322	1251
Dinauyan downstream	SWS-12	7	5	250	260	792
Camgat-Surong	SWS-13	7	8	310	1098	1210
Didipio River	SWS-14	7	9	330	736	869
Camgat River	SWS-15	1	9	310	4251	5485
Surong River	SWS-16	1	9	250	97	471
Dupit River	SWS-17	7	9	330	392	681

15 km (Lobo et al., 2016). It has been suggested that images with higher spatial resolutions between 2 m and 10 m, which are increasingly available, may be applicable for narrower inland waters (Dekker and Hestir, 2012). The objective of this paper is to test this, specifically for small rivers with widths between 4 and 10 m. We develop and evaluate different models to estimate TSS concentrations from surface reflectance over a range of spectral bands. Finally, we used the derived relationship between surface reflectance and TSS to map TSS concentrations throughout the catchment's river network. We conclude by discussing the applicability and limitations of the method.

2. The Didipio Case Study

The Didipio catchment is situated in the northern territory of the Philippines, in the Cagayan Valley province. It has a surface area of 39.25 km², which is made up of the catchments of seven rivers - the Surong, Camgat, Camgat-Surong, Dinauyan, Didipio, Dupit and Alimit rivers (Fig. 1). The rivers are used to support agriculture, including 'kaingin' farming, which strips forested areas to create open lands for grazing. Small-scale gold mining operations became apparent in 2010, coinciding with the developing large-scale Didipio mine. The principal land covers in 2015 were: forest (61%), grassland (23%), open areas (4.2%), residential areas (0.5%), large-scale mining (5.7%) and small-scale mining (0.2%) (Isidro et al., 2017).

TSS measurements were available from eight monitoring stations (Fig. 1), obtained from the large-scale mine's database. The monitored river sections, being located in upland areas, have narrow top-widths and shallow depths (Table 1).

As shown in Fig. 1, the DP-UP station monitors the upper Dinauyan river with DP-DOWN further down the same river and SWS-12 near the confluence with the Camgat-Surong river. SWS-13 monitors the Camgat-Surong river just upstream of the confluence with the Dinauyan river, and SWS-14 monitors after the confluence, at the start of the Didipio river. Between 2015 and 2016, SWS-14 was moved to a section of the Didipio river before the confluence with the Dupit river. SWS-16 is at the outlet of the Surong river, SWS-15 is further up the Camgat river, and SWS-17 is on the Didipio river downstream of the confluence with the Dupit river. The sampling at these stations was scheduled between 9:00 AM and 11:30 AM, which is close to the time of the satellite images (see next section). Table 1 presents the means and standard deviations of the TSS measurements for each of the stations from 2013 to 2016.

3. Methods

3.1. Satellite imagery selection

The selection of satellite imagery was based on identification of images with suitable spatial resolution and acquisition times. Securing at least one pixel completely within the river top-width was preferred. An image with 2 m × 2 m pixels or smaller can easily satisfy this criterion at all sampled river sections. An image with 4 m × 4 m pixels or 6 m × 6 m pixels in some cases creates an overlap with selected river banks (e.g. DP-UP, DP-DOWN, SWS-12), but such an image was

included for comparison. A 10 m × 10 m pixel was considered too large. The image acquisition time needed to coincide as closely as possible with the period of in-situ TSS sampling. Supplementary considerations include the sensor incident angle from nadir and the percentage of cloud coverage. A lower deviation of the incident angle from nadir can reduce geometric errors during image orthorectification (Geometric Distortion in Imagery, 2015). The presence of clouds or their shadows can obscure features on the ground, and reflectance values can be affected towards the edge of a cloud (Wen et al., 2006).

Images were obtained from Pleiades-1A, SPOT-6 and the RapidEye satellite system. Pleiades-1A, SPOT-6 and RapidEye have spatial resolutions of 2 m, 6 m and 5 m respectively. The images cover both the visible (e.g. blue, green and red) and near-infrared spectral bands. The RapidEye satellites do not provide panchromatic images, whereas Pleiades-1A and SPOT-6 do. For the purpose of inter-satellite comparison, only the four major spectral bands (e.g. blue, green, red and near-infrared) were used in this study.

Two Pleiades-1A satellite images, four RapidEye images and one SPOT-6 image were chosen on dates when all the monitoring stations were visible (Table 2). Other available images for the study location were not used due to their lower spatial resolution, high levels of cloud coverage, or deviance in time from the in-situ measurement schedule. For each of the seven images, at least five out of the eight in-situ measurement stations (Table 1) provide near-coincident TSS values.

The SPOT-6 image was captured at the beginning of the dry season whereas the Pleiades-1A and RapidEye images were captured during the middle of the dry season. During the dry season, the low baseflow typical of mountain rivers (Lopez and Justribo, 2010), together with the small catchment areas, mean that both the depths and cross-sectional areas of the river flow were low (Arsen et al., 2014). For example, based on the ground data from 05 May 2014, the water depths at SWS-12, SWS-13 and SWS-14 were approximately 250 mm, 250 mm and 350 mm. It can be assumed that the measured river top-widths in Table 1 are near the annual minimum values. The selected satellites pass directly over the case study area between 08:00:00 AM and 11:30:00 AM. every day; however, the exact image capture time (see Table 2) is also affected by the need to minimize cloud cover. The original image spatial resolution was used rather than pansharping as this may alter reflectance values (Zhang and Roy, 2016).

Table 2
Specifications of selected satellite images.

Imagery	Acquisition time		Spatial resolution (m)		Sensor angle	Cloud cover
	Date	Time	MS	PAN	Degrees	(%)
Pleiades-1A	20-Mar-13	10:45:53 AM	2	0.5	23.74	1.2
	5-May-14	10:35:14 AM	2	0.5	4.89	1
SPOT-6	6-Jan-16	10:09:28 AM	6	1.5	11.93	2
RapidEye	20-Mar-14	11:29:05 AM	5	n.a	12.36	0
	6-Mar-15	11:18:00 AM	5	n.a	7.04	0
	13-Apr-16	10:57:41 AM	5	n.a	10.93	0
	2-May-16	10:56:36 AM	5	n.a	11.69	0

Table 3

List of available monitoring stations for each image.

Imagery	Date	Monitoring stations
Pleiades-1A	20-Mar-13	DP-UP, DP-DOWN, SWS-12
	5-May-14	DP-UP, DP-DOWN, SWS-12, SWS-13, SWS-14
SPOT-6 RapidEye	6-Jan-16	SWS-13, SWS-14, SWS-15, SWS-16, SWS-17
	20-Mar-14	DP-UP, DP-DOWN, SWS-12, SWS-13, SWS-14
	6-Mar-15	SWS-12, SWS-13, SWS-14
	13-Apr-16	SWS-13, SWS-14, SWS-15, SWS-17
	2-May-16	SWS-13, SWS-14, SWS-17

Furthermore, DP-UP, DP-DOWN and SWS-12 stations were detectable in years 2013 and 2014 using Pleiades-1A and RapidEye, but were not within the spatial capacity of SPOT-6 and RapidEye in 2016 as adjacent vegetation (e.g. tall trees) reduced their visible horizontal areas.

3.2. Image calibration

The selected images were preprocessed at level 3 by the providers. Orthorectification and georeferencing were performed through the application of both ground control points and a digital elevation model. This resulted to orthorectified images, which then were subject to radiometric calibration. Radiometric calibration was conducted in two stages. Firstly, the pixel brightness values were normalised by converting the unitless digital numbers into radiance using Eq. (1) (Planet, 2016; Astrium, 2012; Astrium, 2013; Chander et al., 2009). The values of gain and bias are provided in the metadata that accompany the images. Secondly, the radiance was calibrated into top-of-atmosphere reflectance (Eq. (2)) (Astrum, 2013) to adjust for variations in nadir angle and earth to sun distance (Eq. (3)) (Gebreslasie et al., 2010). Lastly, a simple Dark Object Subtraction (DOS) technique, better known as the darkest pixel method, was used to reduce reflectance residuals due to atmospheric interference. This method presumes the existence of objects that have near-zero reflectance (e.g. deep water, dense forest, dark roofs), so that any measured reflectance from these objects is the product of atmospheric interference (Ding et al., 2015). By reviewing the histogram of each spectral band, the pixel from each spectral band with the lowest reflectance value was identified. That value was subtracted from all reflectance values from the corresponding spectral band (Syahreza et al., 2012).

$$L_{\lambda} = \frac{Q_{cal}}{GAIN} + BIAS = Q_{cal} * \text{Scaling factor} \quad (1)$$

$$P_{\lambda} = \frac{\pi \cdot L_{\lambda} \cdot d^2}{ESUN \cdot \cos(\theta_{SZ})} \quad (2)$$

$$d = 1 - 0.01672 \cos[0.9856(JD - 4)] \quad (3)$$

$$\theta_{SZ} = 90^{\circ} - \theta_{SE} \quad (4)$$

where L_{λ} = spectral radiance; Q_{cal} = digital number; P_{λ} = top of atmosphere reflectance; $ESUN$ = solar irradiance; d = earth-sun distance; JD = Julian date; θ_{SZ} = sun zenith angle; θ_{SE} = sun elevation angle.

3.3. Empirical model of the relationship between surface reflectance and TSS

Different models were tested to determine the relationship between TSS and reflectance (Eqs. (5), (6), (7)). These models include linear regression model, power and exponential equations. The data corresponding to images from Pleiades-1A and SPOT-6 were used for spectral analyses, and further combined with the datasets provided by RapidEye for model assessment after consistency verification (Lobo et al., 2016).

$$\text{Regression model} \quad TSS = A_0 + A_1 \cdot S_i + A_2 \cdot S_i^2 \quad (5)$$

$$\text{Power model} \quad TSS = A_1 S_i^{A_0} \quad (6)$$

$$\text{Exponential model} \quad TSS = A_1 e^{S_i} \quad (7)$$

TSS = modeled value of total suspended solids (mg L^{-1}); A_0, A_1, A_2 = parameters; S_i = surface reflectance of selected spectral band.

Model errors were examined by plotting the reflectance data against measured and modelled TSS measurements for each band. The value of the coefficient of determination (R^2) was determined by plotting the observed TSS measurements against their corresponding predicted values. The root mean square error (RMSE) was used to determine the deviation of the modeled value of TSS from the actual measurement. For this task, 28 measurements of TSS were available to estimate the parameters A_0, A_1 and A_2 (Table 3).

3.4. Quantifying within-site variance in spectral signature

Six adjacent Pleiades-1A pixels and three adjacent SPOT-6 and RapidEye pixels were assigned to each monitoring station (Fig. 2). These test pixels were used to examine the local scale variability of

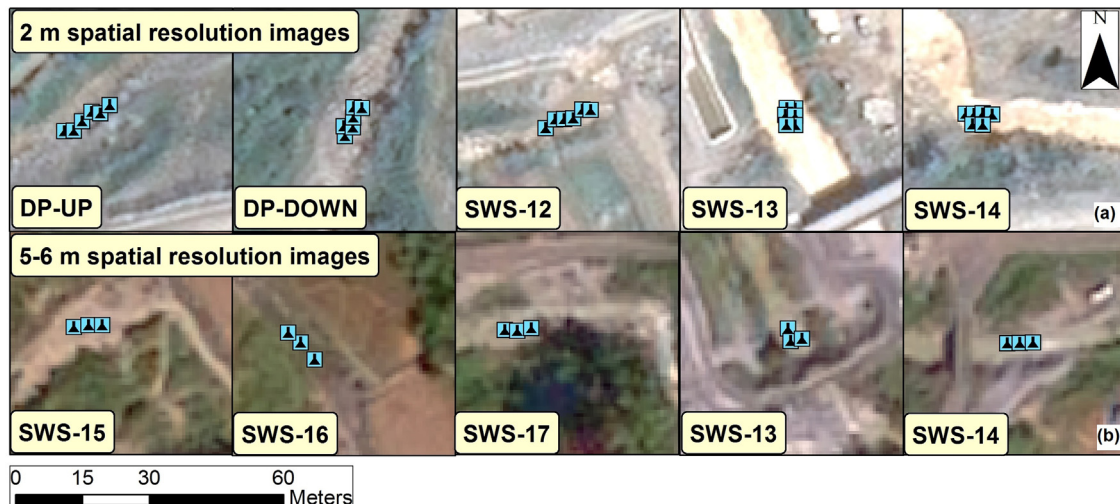


Fig. 2. Locations of the test pixels for each monitoring station and each satellite sensor. (a) Pleiades-1A satellite; (b) SPOT-6 and RapidEye satellites.

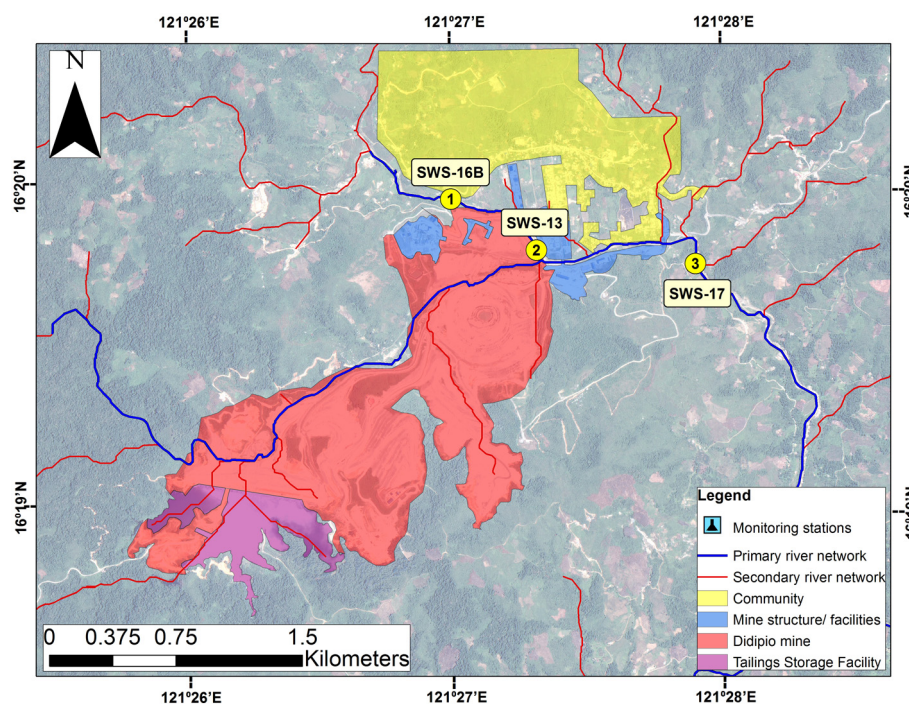


Fig. 3. Assigned stations for the analysis of river turbidity time-variation. Pleiades: © CNES (2013), Distribution Airbus DS/Spot Image.

surface reflectance that may occur due to variations in properties such as river depth and river bottom brightness and thus address issues associated with the spatial resolution of the image. Each of the pixels was within the water top-width. Only a single image from each satellite was used for this test.

3.5. Quantifying potential errors associated with sampling times

TSS sampling was performed from upstream to downstream. Therefore, in the 2013 and 2014 sampling, the DP-UP and DP-DOWN stations were sampled first (near 9.00 AM) and have the greatest deviation from the image acquisition times; and SWS-12, SWS-13 and SWS-14 were the last to be sampled and have the smallest deviation from the image

acquisition times. In 2016, SWS-15 and SWS-16 were sampled first (also near 9.00 AM).

The short-term variations in TSS around the image acquisition times are unknown; however the scope for error due to this variation was investigated during fieldwork in July 2016. Additional, hourly turbidity measurements were made at SWS-16B, SWS-13 and SWS-14 (Fig. 3) using a multi-parameter meter (Horiba U-5000). The intensity of rainfall was recorded as being either light or heavy, and the presence of small-scale mining activity was also noted to assist in interpreting any observed changes in turbidity. The hour to hour variation of turbidity was analysed to assess potential error associated with the image acquisition time deviating from the in-situ sample acquisition. The July 2016 measurements do not necessarily reflect the time variations in TSS on all

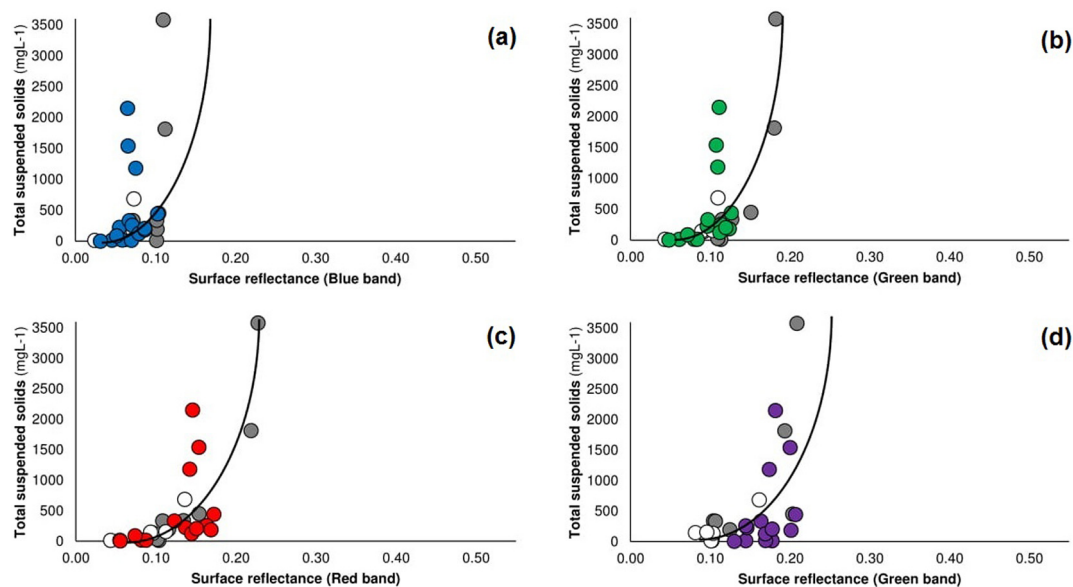


Fig. 4. Graphs of TSS against band reflectance for all the images. (a) blue band; (b) green band; (c) red band; and (d) near-infrared band. Pleiades-1A observations in grey dots; SPOT-6 observations in white dots; and RapidEye in coloured dots. (For interpretation of the references to colour in this figure legend, the reader is referred to the web version of this article.)

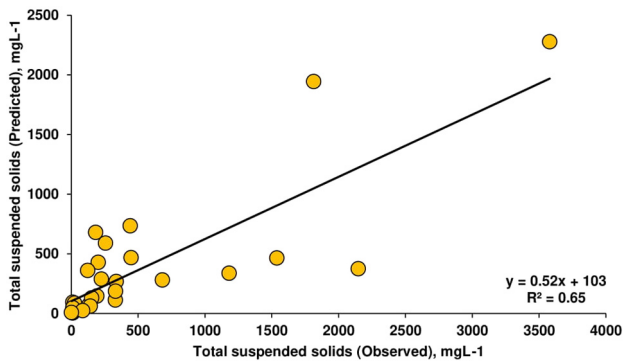


Fig. 5. Plot of observed and estimated values of TSS.

the image acquisition dates. They are likely to over-estimate the degree of variation due to the greater variability of rainfall in July (the start of the wet season) than on the acquisition dates; nevertheless, they are useful as an indication of the possible degree of error associated with the non-coincidence of images and ground-based measurements.

3.6. Analysis of variations in spectral signatures

The spectral signature (surface reflectance profile across the four spectral bands) was plotted for each station and satellite image. This allows a visual analysis of the effects of TSS, river objects, and other aspects of sampling conditions on the spectral signatures, as well as the local-scale variation. The spectral analysis results, as well as the empirical analysis described in Section 3.3, contributed to the selection of the spectral band that best characterises TSS.

To illustrate the potential applicability of the research, the relationship between red band reflectance and TSS based on the derived model from the images was used to translate the surface reflectance map of Pleiades-1A image in 2014 into TSS values. The TSS values in the generated thematic map were divided into increments of 250 mg L^{-1} and a specific pixel colour was assigned for each TSS range.

4. Results and discussion

4.1. Empirical model of the relationship between surface reflectance and TSS

Fig. 4 presents the power law relationship between surface reflectance and TSS concentration for the four spectral bands. The plots are comparable to one another; however, blue, green and near-infrared

bands have lower coefficients of determination (R^2) and the near-infrared band is especially poor at lower TSS levels (e.g. 300 mg L^{-1} and below). This is presumed to be related to interference from protruding rocks at shallow water depths. It is expected that the impact of river bottom will be apparent in the blue and green bands for the shallow depths encountered (Han and Rundquist, 2007), hence surface reflectance in the red band should be more reliable for estimating TSS. A coefficient of determination equal to 65% and RMSE equal to 519 mg L^{-1} were acquired from the plot of observed and estimated values of TSS in Fig. 5, which corresponds to the red band power law model (Eq. (6)). The results in Fig. 4 and Fig. 5 also show the consistency of the power law relationship over the seven images. Within the range of TSS values included in the power law model, the results do not show evidence that using a pixel size of $4 \text{ m} \times 4 \text{ m}$ or $6 \text{ m} \times 6 \text{ m}$ is unsuitable for rivers of widths 4–10 m.

$$\text{TSS} = 947,579 S^{4.07} \quad (6)$$

4.2. Within site variance in spectral signature

Fig. 6 shows that the magnitude of surface reflectance is similar over the six test pixels at each station. The spectral signatures for lower TSS concentrations (e.g. 10 mg L^{-1} at SWS-16 in 2016, 12 mg L^{-1} at DP-UP in 2013, 11 mg L^{-1} at DP-UP in 2014) have reflectance values that are comparable across all visible bands, while their reflectance values in the near-infrared band are higher (Fig. 6). Based on comparing these spectral signatures with those of clearer water (at deep sections of the rivers not covered by the monitoring), it can be seen that clear water has lowest reflectance in the near-infrared band, which is in agreement with previous studies (Lodhi et al., 1997; Tolk et al., 2000). The variations in reflectance across the test pixels at each station is likely to be due to the presence of large stones in the water which can increase the reflectance in the near-infrared band. In particular, the higher variation in the near-infrared reflectance at DP-UP, SWS-12 and SWS-16 in the 2013, 2014 and 2016 images can be attributed to objects such as rocks that protrude during low flows.

The mean and standard deviation of reflectance over each set of test pixels (three for the 2014 and 2016 image and six for the 2013 image) for each station are presented in Table 4. Although the standard deviations show significant variations at some stations, they are low compared to the inter-station and inter-year variations (and low compared to model errors presented in Section 4.1). Therefore, only the mean values in Table 4 are considered in further analysis.

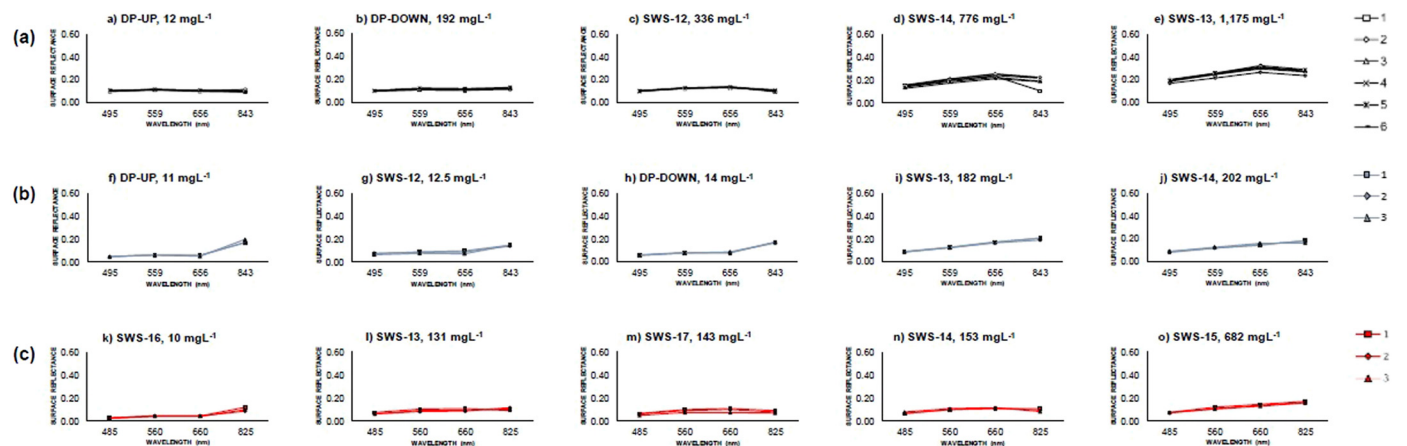


Fig. 6. Plot of surface reflectance from the 6 adjacent pixels at each monitoring station. 2013 Pleiades-1A image: black lines; (b) 2014 RapidEye image: blue lines; (c) 2016 SPOT-6 image: red lines. (For interpretation of the references to colour in this figure legend, the reader is referred to the web version of this article.)

Table 4

Mean and standard deviation of surface reflectance across the six test pixels at each station and corresponding values of TSS.

Stations	Blue band		Green band		Red band		Near infrared band		TSS mg L ⁻¹
	Mean	σ	Mean	σ	Mean	σ	Mean	σ	
Year: 20 March 2013									
DP-UP	0.1015	0.002	0.1135	0.003	0.1038	0.003	0.1024	0.01	12
DP-DOWN	0.1021	0.002	0.1191	0.005	0.1159	0.01	0.1248	0.01	192
SWS-12	0.1017	0.002	0.1272	0.002	0.1345	0.004	0.1042	0.01	336
SWS-13	0.1889	0.01	0.2464	0.02	0.3014	0.02	0.2726	0.02	1175
SWS-14	0.1435	0.01	0.1947	0.01	0.2343	0.02	0.1888	0.04	776
Year: 20 March 2014									
DP-UP	0.0459	0.001	0.0614	0.003	0.0552	0.005	0.1778	0.016	11
DP-DOWN	0.0587	0.002	0.0800	0.002	0.0821	0.004	0.1696	0.003	14
SWS-12	0.0702	0.005	0.0839	0.006	0.0876	0.01	0.1448	0.01	12.5
SWS-13	0.0870	0.002	0.1240	0.003	0.1692	0.005	0.2015	0.009	182
SWS-14	0.0867	0.003	0.1198	0.005	0.1511	0.008	0.1780	0.011	202
Year: 6 January 2016									
SWS-13	0.066	0.008	0.0914	0.01	0.0966	0.01	0.1035	0.01	131
SWS-14	0.072	0.005	0.1033	0.00	0.1127	0.00	0.0960	0.01	153
SWS-15	0.041	0.029	0.0674	0.04	0.0760	0.06	0.1171	0.04	682
SWS-16	0.024	0.001	0.0433	0.00	0.0437	0.00	0.1012	0.02	10
SWS-17	0.061	0.008	0.0895	0.01	0.0937	0.02	0.0816	0.01	143

4.3. Potential errors associated with sampling times

The hourly time-series of turbidity show that there were significant variations of turbidity around the sampling times. These variations were greater when rainfall was noted, and one observation implied that the greatest time variation is due to rainfall coinciding with small-scale mining activity; however, the variation of turbidity in the presence of mining activities and absence of rainfall is minimal (Fig. 7). Although this hourly analysis was not done on either of the image capture dates, it may be used to indicate the potential error associated with short-term fluctuations around the sampling time.

Fig. 7 indicates that the measurement error associated with a transition from no anthropogenic activities to small-scale mining activity can be ± 37 NTU or equivalent to 27 mg L^{-1} based on the relationship between turbidity and TSS of the rivers.

4.4. Analysis of variations in spectral signatures

Fig. 8 shows the spectral signature for all five sampling locations using all the seven images for the purpose of comparing the 2013, 2014 and 2016 signatures. Based on visual assessment, there is a general increase in reflectance at all spectral bands as TSS level increases, and Fig. 4 shows that this is relatively linear up to approximately 500 mg L^{-1} . In contrast, over higher TSS levels, reflectance increases at a generally lower and more variable rate. Where reflectance in the near-infrared band is higher than in the red band (particularly Fig. 8c), this indicates that protruding rocks and dark river bottom suppresses the reflectance of suspended solids because near-infrared waves are expected to be absorbed by water (Khorram et al., 2012).

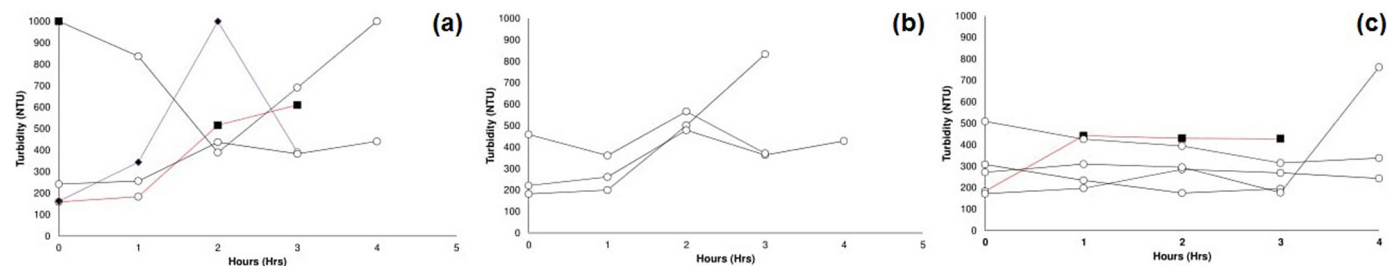


Fig. 7. Time variation in turbidity (NTU). (a) Shaded square in red line: small-scale mining activity noted nearby upstream but no rainfall; (b) shaded diamond in purple line: rainfall and small-scale mining activity noted nearby upstream; (c) white circle: rainfall noted but no small-scale mining activity. (For interpretation of the references to colour in this figure legend, the reader is referred to the web version of this article.)

4.5. Mapping TSS concentrations

Eq. 6 was used to calibrate river pixels in the Pleiades-1A image to TSS values. Fig. 9 shows the example for the date of the 2014 image focusing on the length of the Camgat-Surong river from its origin at the confluence of the Camgat and Surong rivers downstream to its confluence with the Dinauyan. The model discussed above allows mapping of TSS values fairly accurately only over the range $0\text{--}500 \text{ mg L}^{-1}$.

The map assists with reporting the spatial variations in TSS and degree of attribution to different land uses. For example, Fig. 9 illustrates the relatively low TSS values in the upper Dinauyan river, which may be associated with the low small-scale gold mining activity in that river and dominance of grassland. In contrast, a hydraulic small-scale mine operates on the lower Dinauyan, which may be the reason for the strong transition in TSS on that river. The Camgat and Camgat-Surong exhibits generally high TSS concentrations, associated with more active small-scale mining. As well as examining such spatial variations in TSS, differences between maps may be plotted to highlight river reaches where changes have occurred, although the confidence with which change could be detected and attributed would be affected by the low temporal resolution of the images.

5. Conclusions

RapidEye satellite images and near-simultaneous ground measurements of TSS were used to evaluate the applicability of satellite images for mapping TSS concentrations in small (4–10 m top width, 250–330 mm depth) mountain rivers. A separate dataset from Pleiades-1A and SPOT-6 satellite images gave consistent results. TSS and surface reflectance are linearly related for ranges of TSS from

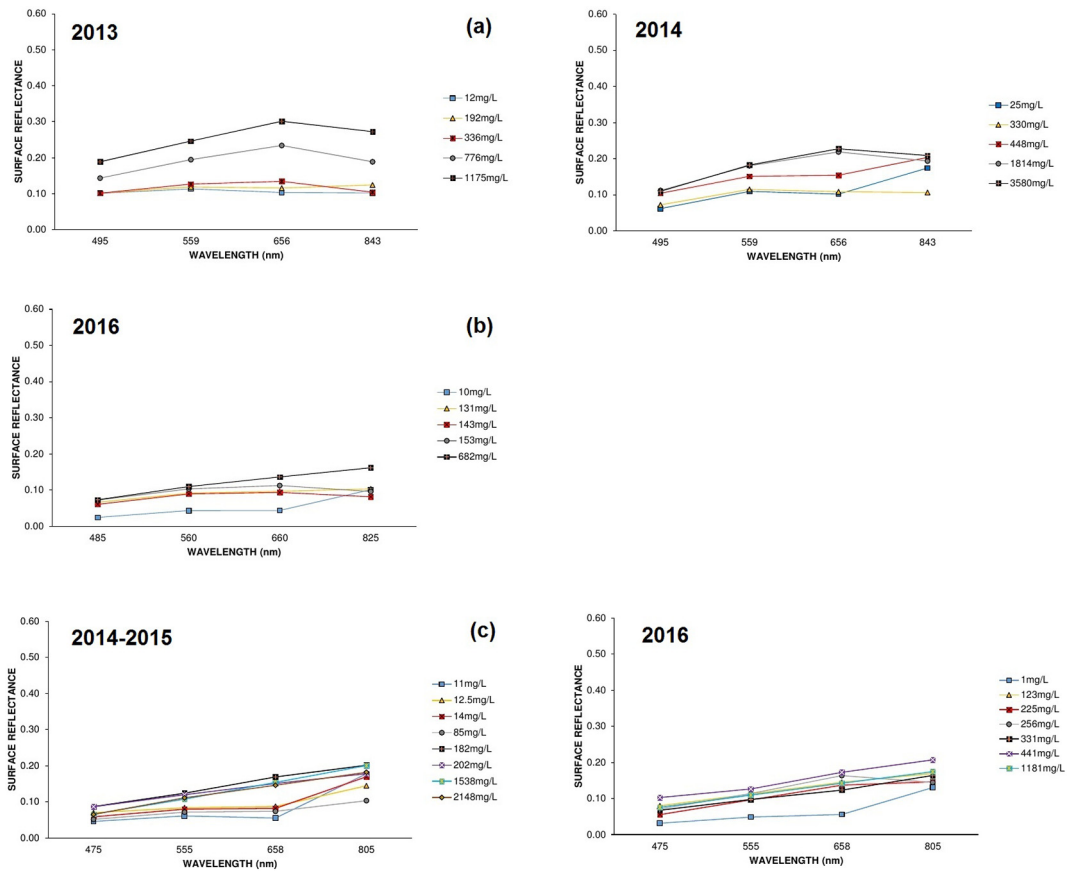


Fig. 8. Spectral signatures of water for different concentrations of TSS (a) 2013–2014 Pleiades-1A; (b) 2016 SPOT-6; (c) 2014–2016 RapidEye.

1 mg L^{-1} to approximately 500 mg L^{-1}); however, a power function better described reflectance and TSS ranging from 1 mg L^{-1} to 3580 mg L^{-1} . TSS has a particularly strong correlation with the red band reflectance, with $R^2 = 65\%$. Lower R^2 values were obtained using

the other spectral bands, which may be associated with sensitivity of reflectances in these bands to protruding rocks and dark bottom of shallow rivers. While using images with a pixel size of $2 \text{ m} \times 2 \text{ m}$ or less is recommended for the studied river widths ($4\text{--}10 \text{ m}$), the image with

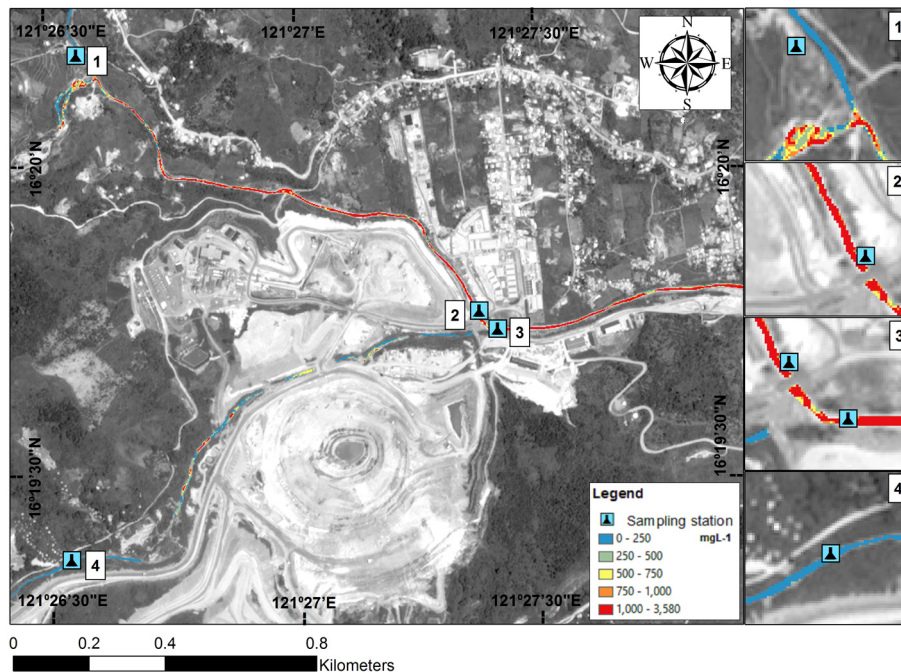


Fig. 9. Map of estimated TSS concentration for Pleiades-1A 05 May 2014 image. (a) panel 1: Camgat River at lower left and Surong River at upper right; (b) panel 2: Camgat- Surong River; (c) panel 3: Didipio River; (d) panel 4: Dinauyan River.

a 5 m × 5 m or 6 m × 6 m pixel size gave comparable results in this case. The model can assist in spatial analysis of the effect of land use features on river water quality, including those features that are distant from water quality monitoring stations. However, the model is restricted by the ranges and sources of TSS at the image acquisition times, and still requires further TSS data from the upper bound to better predict the full range of TSS variations within the Didipio catchment.

Acknowledgments

This research was undertaken partly through the funding provided by the Australia Awards Scholarship (2015–2017), Sustainable Minerals Institute Support Grant (2016–2017) and the Australian Research Council under the Future Fellowship program (Project ID: FT140100977). In addition, the authors would like to acknowledge OceanaGold (Philippines) Incorporated Environmental Team, the International River Foundation (IRF) and the Mines and Geosciences Bureau (MGB), Region II for the permission to access their database of water quality; the Airbus Defence and Space for the acquisition of Pleiades-1A satellite images in March 2013 and 2014 and SPOT-6 in January 2016, and Planet Constellation for the provision of RapidEye images.

References

- Arsen, A., Cretaux, J.-F., Berge-Nguyen, M., Abarca del Rio, R., 2014. Remote sensing-derived bathymetry of Lake Poopo. *Remote Sens.* 12 (4):407–420. <https://doi.org/10.3390/rs6010407>.
- Astrum, 2012. Pleiades Imagery User Guide. Retrieved from. <http://www.cscrs.itu.edu.tr/assets/downloads/PleiadesUserGuide.pdf>.
- Astrum, 2013. SPOT 6 & SPOT 7 Imagery User Guide.
- Baker, E.T., Lavelle, J.M., 1984. The effect of particle size on the light attenuation coefficient of natural suspensions. *J. Geophys. Res.* 89 (C5):8197–8203. <https://doi.org/10.1029/JC089iC05p08197>.
- Chander, G., Markham, B.L., Helder, D.L., 2009. Summary of current radiometric calibration coefficients for Landsat MSS, TM, ETM+, and EO-1 ALI sensors. *Remote Sens. Environ.* 113 (5):893–903. <https://doi.org/10.1016/j.rse.2009.01.007>.
- Dekker, A.G., Hestir, E.L., 2012. Evaluating the Feasibility of Systematic Inland Water Quality Monitoring With Satellite Remote Sensing. CSIRO: Water for a Healthy Country National Research Flagship.
- Ding, H., Shi, J., Wang, Y., Wei, L., 2015. An Improved Dark-object Subtraction Technique for Atmospheric Correction of Landsat-8. 9815:pp. 1–8. <https://doi.org/10.1117/12.2205567>.
- Gebreslasie, M.T., Ahmed, F.B., van Aardt, J.A., 2010. Image-based reflectance conversion of ASTER and IKONOS imagery as precursor to structural assessment of plantation forests in KwaZulu-Natal, South Africa. *Southern Forests* 71 (4):259–265. <https://doi.org/10.2989/SF.2009.71.4.2.1029>.
- Gitelson, A., Garbuzov, G., Szilagyi, F., Mittenzwey, K.-H., Karnieli, A., Kaiser, A., 1993. Quantitative remote sensing methods for real-time monitoring of inland waters quality. *Int. J. Remote Sens.* 14 (7):1269–1295. <https://doi.org/10.1080/01431169308953956>.
- Han, L., Rundquist, D., 2007. Spectral characterization of suspended sediments generated from two texture classes of clay soil. *Int. J. Remote Sens.* 17:643–649. <https://doi.org/10.1080/01431169608949034>.
- Harrington Jr., J.A., Schiebe, F.R., Nix, J.F., 1992. Remote sensing of Lake Chicot, Arkansas: monitoring suspended sediments, turbidity, and Secchi depth with Landsat MSS data. *Remote Sens. Environ.* 39 (1):15–27. [https://doi.org/10.1016/0034-4257\(92\)90137-9](https://doi.org/10.1016/0034-4257(92)90137-9).
- Hellweger, F., Schlosser, P., Lall, U., Weissel, J., 2004. Use of satellite imagery for water quality studies in New York Harbor. *Estuar. Coast. Shelf Sci.* 61:437–448. <https://doi.org/10.1016/j.ecss.2004.06.019>.
- Isidro, C.M., McIntyre, N., Lechner, A.M., Callow, I., 2017. Applicability of earth observation for identifying small-scale mining footprints in a wet tropical region. *Remote Sens.* 9: 945–967. <https://doi.org/10.3390/rs9090945>.
- Khorram, S., Nelson, S.A., Koch, F.H., van der Wiele, C.F., 2012. Remote Sensing. Springer, New York, United States of America <https://doi.org/10.1007/978-1-4614-3103-9>.
- Liew, S.-C., Lu, X.-X., Chen, P., Zhou, Y., 2003. Remote Sensing of Suspended Sediment Concentrations in Highly Turbid Inland River Waters: An Example From the Lower Jinsha Tributary, Yunnan, China. <https://courses.nus.edu.sg/course/geoluxx/notes/Liew%20et%20al%20rs%20of%20SSC.pdf>.
- Lobo, F.L., Costa, M., Novo, E.M., Telmer, K., 2016. Distribution of artisanal and small-scale gold mining in the Tapajos River Basin (Brazilian Amazon) over the past 40 years and relationship with water siltation. *Remote Sens.* 8 (579). <https://doi.org/10.3390/rs8070579>.
- Lodhi, M.A., Rundquist, D.C., Han, L., Kuzila, M.S., 1997. The potential for remote sensing of loess soils suspended in surface waters. *J. Am. Water Resour. Assoc.* 33 (1):111–117. <https://doi.org/10.1111/j.1752-1688.1997.tb04087.x>.
- Lopez, R., Justribo, C., 2010. The hydrological significance of mountains: a regional case study, the Ebro River basin, northeast Iberian Peninsula. *Hydrol. Sci. J.* 55 (2): 223–233. <https://doi.org/10.1080/02626660903546126>.
- Planet, 2016. RapidEye Imagery Product Specifications. Retrieved from. <https://www.planet.com/products/satellite-imagery/files/160625-RapidEye%20Image-Product-Specifications.pdf>.
- Pusch, R., Yong, R.D., Nakano, M., 2012. Origin and function of soils. *Environmental Soil Properties and Behaviour*. Taylor & Francis Group, Boca Raton, pp. 1–24.
- Rugner, H., Schwientek, M., Beckingham, B., Kuch, B., Grathwohl, P., 2013, February 17. Turbidity as a proxy for total suspended solids (TSS) and particle facilitated pollutant transport in catchments. *Environ. Earth Sci.*:373–380 <https://doi.org/10.1007/s12665-013-2307-1>.
- Syahreza, S., Matjafri, M.Z., Lim, H.S., Mustapha, M.R., 2012. Water quality assessment in Kelantan Delta using remote sensing technique. *Electro-Optical Remote Sensing, Photonic Technologies, and Applications VI*. 85420X. <https://doi.org/10.1117/12.978931>.
- Tindall, J.A., Kunkel, J.R., 2009. Physical properties and characteristics of soils. In: Tindall, J.A., Kunkel, J.R. (Eds.), *Unsaturated Zone Hydrology*. Prentice Hall.
- Tolk, B.L., Han, L., Rundquist, D.C., 2000, November 25. The impact of bottom brightness on spectral reflectance of suspended sediments. *Int. J. Remote Sens.* 21 (11): 2259–2268. <https://doi.org/10.1080/01431160050029558>.
- Wang, J.J., Lu, X.X., 2010. Estimation of suspended sediment concentrations using Terra MODIS: an example from the lower Yangtze River, China. *Sci. Total Environ.* 408: 1131–1138. <https://doi.org/10.1016/j.scitotenv.2009.11.057>.
- Wang, J.-J., Lu, X.-X., Zhou, Y., Liew, S.-C., 2012. Suspended sediment concentrations estimate in highly turbid rivers: a field spectral survey. *Remote Sensing Letters*:409–417 <https://doi.org/10.1080/2150704X.2012.743689>.
- Wen, G., Marshak, A., Cahalan, R.F., 2006. Impact of 3-D clouds on clear-sky reflectance and aerosol retrieval in a biomass burning region of Brazil. *IEEE Geosci. Remote Sens. Lett.* 3 (1):169–172. <https://doi.org/10.1109/LGRS.2005.861386>.
- Wu, J.-L., Ho, C.-R., Huang, C.-C., Srivastav, A.L., Tzeng, J.-H., Lin, Y.-T., 2014, November 28. Hyperspectral sensing for turbid water quality monitoring in freshwater rivers: empirical relationship between reflectance and turbidity and total solids. *Sensors* 14: 22670–22688. <https://doi.org/10.3390/s14122670>.
- Zhang, H.K., Roy, D.P., 2016. Computationally inexpensive Landsat 8 Operational Land Imager (OLI) pansharpening. *Remote Sens.* 8 (3):190. <https://doi.org/10.3390/rs8030180>.